Nanostructured Li_2MnSiO_4/C Cathodes with Hierarchical Macro-/Mesoporosity for Lithium-Ion Batteries

*Guang He and Arumugam Manthiram**

Li_2MnSiO_4/C nanocomposite with hierarchical macroporosity is prepared with poly(methyl methacrylate) (PMMA) colloidal crystals as a sacrificial hard-template and water-soluble phenol-formaldehyde (PF) resin as the carbon source. Scanning electron microscopy (SEM) and transmission electron microscopy (TEM) analyses confirm that the periodic macropores are ≈400 nm in diameter with 20–40 nm walls comprising Li_2MnSiO_4/C nanocrystals that produce additional large mesopores (< 30 nm) between the nanocrystals. The nanostructured Li_2MnSiO_4/C cathode exhibits a high reversible discharge capacity of 200 mAh g^{-1} at C/10 (16 mA g^{-1}) rate at 1.5–4.8 V at 45 °C. Although the discharge capacity can be further increased on operating at 55 °C, the sample exhibits a relatively fast capacity fade at 55 °C, which can be partially solved by simply narrowing the voltage window to avoid side reactions of the electrolyte. The good performance of the Li_2MnSiO_4/C cathodes is attributed to the unique macro-/mesostructure of the silicate coupled with uniform carbon coating.

1. Introduction

With more than two decades of development and evolution, lithium-ion batteries have become the dominant power source for portable electronic devices. However, the utilization of the lithium-ion technology for electric vehicles (EVs) and grid storage of electricity produced by renewable energies is hampered by limitations in energy, power, and cycle life, high cost, and safety concerns. For example, the layered $LiCoO_2$ cathode allows a reversible extraction/insertion of only ≈0.5 lithium per formula unit, suffers from serious safety concerns due to oxygen release from the lattice under conditions of overcharge,[1,2] and is expensive, making it unsuitable for large-cell applications necessary for EVs or grid storage. With an aim to increase the energy density, lower the cost, and improve the thermal stability, polyanion cathodes,[3,4] particularly Li_2MSiO_4 (M = Mn, Fe, and Co) that has the potential to reversibly extract/insert two lithium ions per transition-metal ion,[5] have become appealing. The Li_2MSiO_4 family of cathodes adopts the Li_3PO_4-type structure in which the transition-metal ions are located in tetrahedral sites.

Dr. G. He, Prof. A. Manthiram
Materials Science and Engineering Program & Texas Materials Institute
The University of Texas at Austin
Austin, TX 78712, USA
E-mail: manth@austin.utexas.edu

DOI: 10.1002/adfm.201400610

Among the three Li_2MSiO_4 (M = Mn, Fe, and Co) cathodes, Li_2FeSiO_4 shows the most stable cycle life.[6–9] Reversible extraction of more than one lithium ion from Li_2FeSiO_4 has been accomplished as indicated by the high capacity of more than 200 mAh g^{-1}. Analysis of the electrodes after fully charging has also suggested the formation of Fe^{4+},[10–12] but controversies exist.[13] Further studies are needed to settle it. The main disadvantage of Li_2FeSiO_4 is the relatively low operating voltage of ≈2.5 V, which reduces the overall energy density. On the other hand, there is still a long way to go for the other two cathodes, i.e., Li_2MnSiO_4 and Li_2CoSiO_4, because of the severe capacity degradation. Bruce et al.[14] systematically studied the structures and electrochemical activities of the three polymorphs (β_{II}, β_I, and γ_0) of Li_2CoSiO_4, among which β_{II}-Li_2CoSiO_4 exhibits the best behavior. About 1.1 Li ions were extracted up to 4.6 V during the first charge, while only ≈0.4 Li could be reversibly inserted at ≈4.0 V. The capacity became negligible after 10 cycles. Similar results have also been reported by other groups even with carbon-coated Li_2CoSiO_4 nanoparticles,[15,16] implying structural rearrangement probably takes place on the first cycle as observed with Li_2MnSiO_4 and Li_2FeSiO_4. Theoretical calculations have predicted that the reaction of the Co^{3+}/Co^{4+} couple should occur at 4.8 V or even higher,[17,18] which is beyond the electrochemical stability window of the currently used carbonate electrolyte systems.

Among the three systems, Li_2MnSiO_4 offers the possibility to deliver the highest reversible capacity within an acceptable voltage-stability window due to the fact that Mn^{4+} is more stable and accessible than Co^{4+} and Fe^{4+}.[19] The main challenge with Li_2MnSiO_4 is the poor cyclability caused by the inherent instability of Mn^{3+} along with the phase transformation occurring on cycling. The extremely low electrical and ionic conductivities of Li_2MnSiO_4 also have a significant influence on the electrode performance; for example, the electrical conductivity of Li_2MnSiO_4 is in the range of 10^{-14}–10^{-16} S cm^{-1} at room temperature.[20] As a result, only 0.5–0.6 Li ions could be reversibly extracted at a very small current rate of C/30 in an earlier report.[5b] Similar to the evolution of the $LiFePO_4$ cathode, great success has been made with Li_2MnSiO_4 with strategies such as carbon wiring of nanoparticles to improve its conductivity.[21] Furthermore, it has been noted that some Li_2MnSiO_4 cathodes with high carbon content (e.g., >40 wt%) result in better stability, which is attributed to improved kinetics and better

structural stability.[22,23] However, it is obvious that incorporation of too much carbon into the cathode can reduce the overall energy density. Another problem is the difficulty of charge transfer across the interface between the electrolyte and the active material because the pathway for electrolyte percolation can be blocked by additional carbon, especially with the electrodes having particle agglomeration problems.[24]

A possible solution to have a balance between high carbon content and sufficient void space in the electrodes is the fabrication of hierarchical macroporous structures. There are many advantages to this type of electrodes.[25] First, the pore walls of the active material are at nanoscale (tens of nanometers), which reduces the lithium-ion diffusion length. Also, the large and periodic pores could offer a fast permeation rate for the electrolyte in the electrodes and a sufficient electrode/electrolyte interface for ion transfer. More importantly, the abundant porosity can provide the space for particle growth of the active material and prevent the formation of electrolyte-inaccessible cores on cycling. Finally, carbon (or other conductive materials) could be readily incorporated to enhance the electrical conductivity of the electrodes. Some cathode materials with this type of structure have shown enhanced electrochemical performance, but most of them are limited to carbon systems[26] and simple oxide compounds such as V_2O_5,[27,28] and $LiMn_2O_4$.[29] Recently, more complicated configurations such as the $LiFePO_4$ and $LiFePO_4$/C nanocomposite have been successfully prepared by carefully controlling the precursors,[30,31] indicating other polyanion cathodes could possibly be fabricated with similar procedures.

Herein, we present for the first time a one-step synthesis of Li_2MnSiO_4/C nanocomposite with hierarchical macroporosity by employing poly(methyl methacrylate) (PMMA) colloidal crystals as a sacrificial hard-template and water-soluble phenolic resin as a carbon source. No extra washing step is required to remove the template because PMMA spheres decompose to gases below 400 °C in an inert atmosphere. The periodic pores are 380–400 nm in diameter, formed by the walls of Li_2MnSiO_4/C. Additional textual mesoporosity is created in the walls as well as between the Li_2MnSiO_4/C nanocrystals. Electrochemical measurements show high capacity with cycling stability over 100 cycles for the Li_2MnSiO_4/C cathodes at 45 °C. At a higher temperature of 55 °C, it is found that a narrow cycling window is necessary to reduce the influence of electrolyte stability on capacity fading.

2. Results and Discussion

2.1. Structure and Morphology Characterizations

Li_2MnSiO_4 with the $Pmn2_1$ symmetry has the β-Li_3PO_4-type structure that is composed of hexagonal-closed-packed oxide ions with the cations occupying half of the tetrahedral sites. **Figure 1**a shows the structure of Li_2MnSiO_4, where MnO_4 and SiO_4 tetrahedra point in the same direction and run alternately by sharing corners along the a direction. Lithium ions occupy the tetrahedral sites in between the MnO_4 and SiO_4 layers and migrate following a tortuous path with jump distances of 3.1–3.2 Å.[32] The powder X-ray diffraction (XRD) pattern of as-prepared Li_2MnSiO_4/C (Figure 1b) shows that all reflections could be indexed on the basis of an orthorhombic structure with the space group $Pmn2_1$, except for a very small MnO peak at 31° as reported by many other groups.[21c,22,23,33–39] Elemental analysis of the sample by the inductively coupled plasma analysis (ICP) shows a Li:Mn ratio of 1.93:1, indicating a small fraction of lithium evaporation during the pyrolysis at 700 °C. The carbon content in the composite was determined to be ≈20 wt% by thermogravimetric analysis (TGA) under air (Figure S1, Supporting Information).

The synthetic procedure for the ordered macroporous Li_2MnSiO_4/C is illustrated in **Figure 2**a. Poly(methyl methacrylate) (PMMA) colloidal crystals were first synthesized with the close-packed PMMA spheres. Since the Li_2MnSiO_4/C replica is highly dependent on the quality of the PMMA hard-template, the morphology of the PMMA crystal was studied using high-resolution field-emission scanning electron microscopy (FE-SEM). As expected, the crystals are composed of long-range uniform close-packed PMMA spheres with a diameter of approximately 430 nm, as shown in Figure 2b. A highly concentrated precursor solution (≈6 M) was then prepared by dissolving tetraethyl orthosilicate (TEOS), lithium and manganese nitrates, and phenolic resin in sequence. This order is important to prevent any precipitation from the clear viscous solution. Next, the PMMA crystals were immersed into this solution to allow the infiltration of the various precursors into the PMMA crystals. Finally, the template was decomposed by a pyrolysis process to generate the replica of PMMA. The low magnification SEM image of the templated sample (Figure 2c) shows the replica structure with a hierarchical macroporous architecture having open windows. Although a few regions with broken/distortion walls have resulted, the interconnected three-dimensional nanostructure was still preserved after the high-temperature treatment. The average pore size estimated from this SEM image is ≈380–400 nm. It is known that either carbon or silica with ordered macroporosity could be easily prepared under similar conditions using phenol-formaldehyde (PF) resol or TEOS as precursors.[40] Herein, it is necessary to examine the chemical composition of the resulting material. Elemental maps conducted on such a small particle with

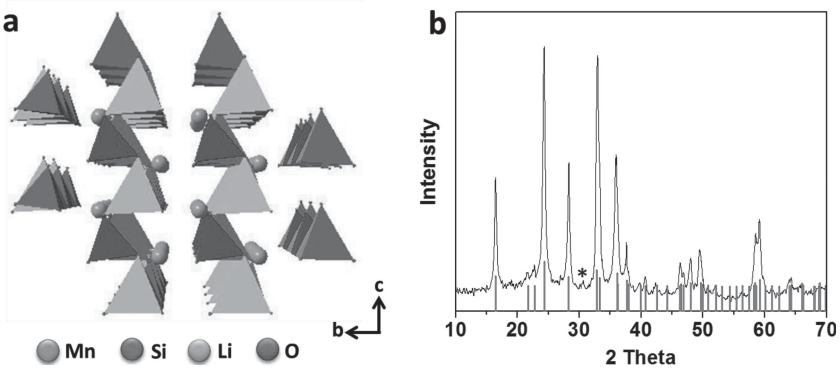

Figure 1. a) Crystal structure of Li_2MnSiO_4 with the space group of $Pmn2_1$, b) XRD pattern of the as-prepared Li_2MnSiO_4/C composite with PMMA as the hard template. The peak labeled with the asterisk corresponds to MnO.

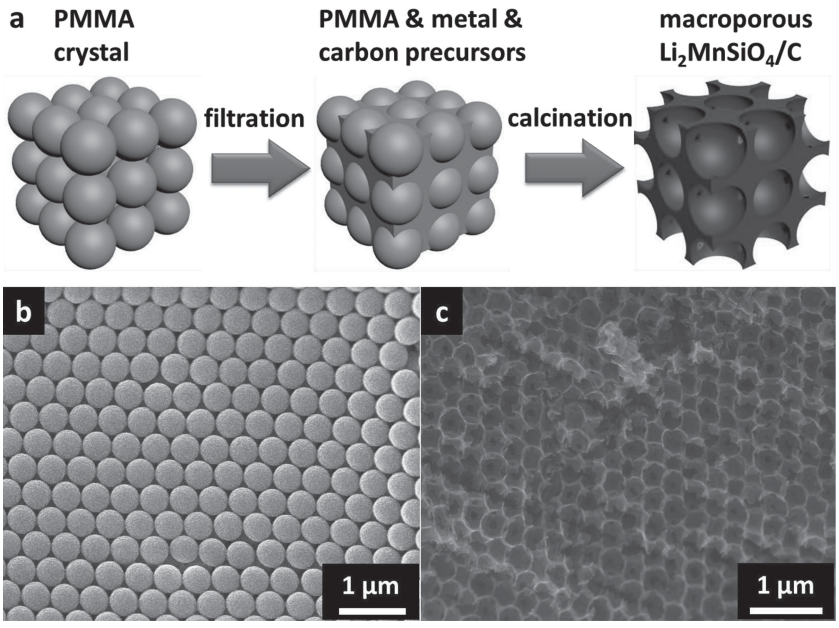

Figure 2. a) Schematic representation of the preparation process of the hierarchical ordered macroporous Li_2MnSiO_4/C with PMMA as the hard template; SEM images of the b) PMMA spheres and c) the resulting Li_2MnSiO_4/C replica.

periodic macropores such as in **Figure 3** display a homogeneous distribution of Mn, Si, O, and C at nanoscale, indicating the formation of Li_2MnSiO_4 with a uniform carbon incorporation. It is also confirmed by the SEM image that the walls surrounding the pores are composed of small nanocrystals with an average thickness of 20–40 nm.

More detailed structural information of the Li_2MnSiO_4/C nanocomposite was collected with transmission electron microscopy (TEM). In **Figure 4**a, the diameters of the three well-recognized pores are 380, 420, and 420 nm, respectively, fairly close to the estimation obtained from the low magnification SEM image. In the TEM image, darker regions are observed in some places. In a similar work[31] on $LiFePO_4/C$ with ordered macroporous structure, the darker regions were ascribed to $LiFePO_4$-rich regions. This conclusion was confirmed by the same group in subsequent work, where combustion of carbon produced separate $LiFePO_4$ spheres.[41] In our experiment, however, the mapping analysis in Figure 3 suggests a uniform elemental distribution. The regions are more likely due to thickness-based contrast[42] rather than separate domains of Li_2MnSiO_4-rich and C-rich regions. The average wall thickness is ≈30 nm as estimated in Figure 4b, which gives an interior pore size of ≈350–380 nm, 15% smaller than the original PMMA sub-micron spheres (Figure 2b, ≈430 nm). Previously reported $LiFePO_4/C$ with similar three-dimensional macropores showed a significant structural shrinkage (≈30%, 290 vs. 400 nm for $LiFePO_4/C$ and PMMA) after thermal treatment at 600 °C.[31] There are two reasons for the different shrinking rates between Li_2MnSiO_4 and $LiFePO_4$. First, it has been realized in recent years that silica could reinforce the porous structure and maintain the pore size during the pyrolysis process when making porous materials.[43] Thus, the hydrolyzed products of TEOS formed as intermediate species (SiO_2 or SiO_4^{4-}) during the preparation of Li_2MnSiO_4 effectively prevent the structural shrinking. Secondly, the copolymer F127 with a high relative ratio in the precursors was employed as a surfactant to increase the porosity of $LiFePO_4/C$. After it was decomposed below 400 °C, a large shrinkage of $LiFePO_4$ was necessary to fill the void space and achieve a stable macroporous structure. Considering both of these factors, a small

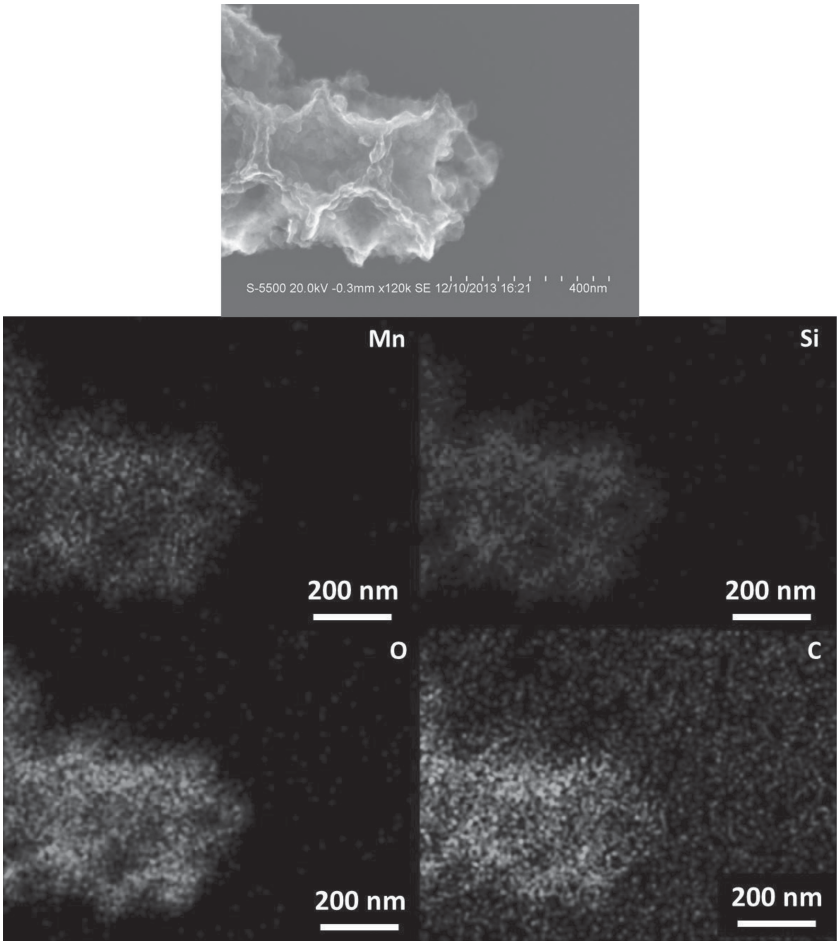

Figure 3. SEM image and elemental maps of Mn, Si, O, and C of a Li_2MnSiO_4/C particle.

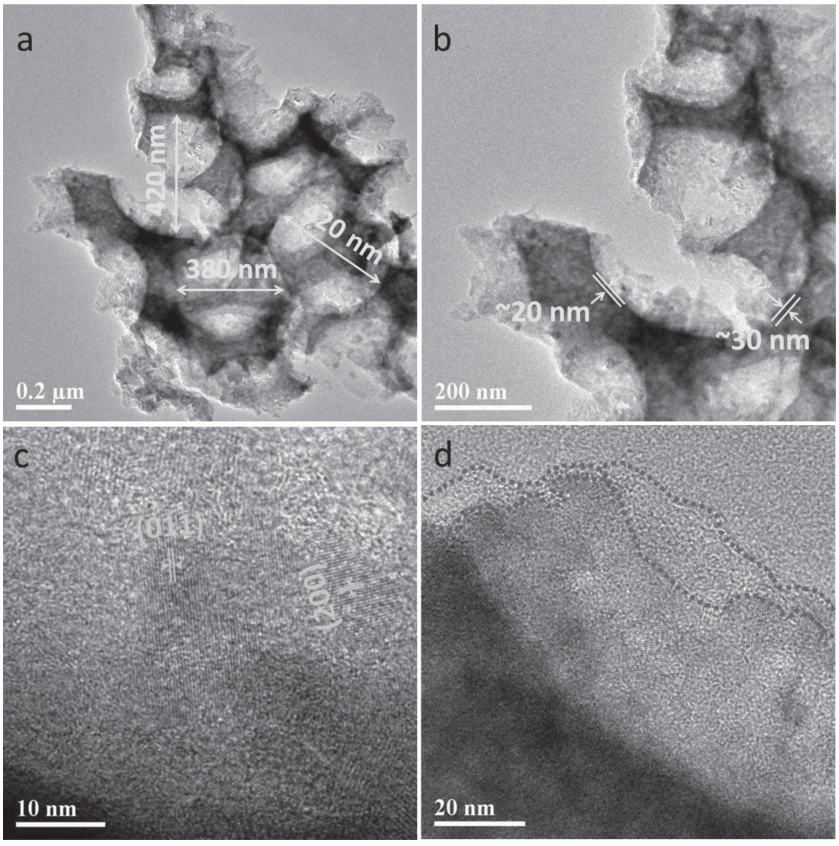

Figure 4. a,b) TEM and c,d) HR-TEM images of the Li_2MnSiO_4/C nanocomposite. The region within the dotted line indicates the carbon layer.

structural shrinkage of 15% for Li_2MnSiO_4 is reasonable in our experiment.

The lattice fringes of Li_2MnSiO_4 are clearly demonstrated in the high-resolution TEM (HR-TEM) image in Figure 4c with a spacing of 0.315 and 0.366 Å, corresponding to the (200) and (011) planes. A carbon-coating layer (the region within the dots) with an average thickness of ≈10 nm is evidenced by the HR-TEM shown in Figure 4d. Raman analysis (Figure S2, Supporting Information) shows both D and G bands with an intensity ratio I_D/I_G of 0.92. A typical G band in graphite is located at ≈1581 cm^{-1}. The small shift to 1595 cm^{-1} in Li_2MnSiO_4/C could be due to the nanocarbon in the composite.[31]

Nitrogen adsorption analysis of Li_2MnSiO_4/C in **Figure 5**a shows little hysteresis in the intermediate relative pressure region ($0.4 < P/P_0 < 0.7$) and a sharp rise of the adsorption branch near unit pressure ($P/P_0 > 0.9$, where P and P_0 are the equilibrium and saturation pressures, respectively). The specific Brunauer–Emmett–Teller (BET) surface area (Figure 5a, inset plot) is 40 m^2 g^{-1}. These features reveal that most of the porosity in Li_2MnSiO_4/C comes from the large mesopores and macropores. The pore size distribution curve based on the quenched solid density functional theory (QS-DFT) method demonstrates a broad peak at 16 nm (Figure 5b), which is probably a reflection of the pores caused by the aggregation of the Li_2MnSiO_4/C nanodomains (20–30 nm, as shown in Figure 3). Combined with the SEM data, it is clear that the Li_2MnSiO_4/C nanocomposite has a bimodal nanostructure with both interconnected hierarchical macropores and disordered mesopores. The macropores are templated by the PMMA colloidal crystals with active material walls, while the mesopores derive from the voids between the Li_2MnSiO_4/C nanocrystals in the walls. This unique architecture could significantly reduce the lithium-ion diffusion pathways within the cathode. More importantly, the large periodic macropores are completely accessible to the electrolyte owing to the open windows, which greatly facilitates lithium-ion transfer through the liquid/solid (electrolyte/cathode) interface. In addition, the large macropores provide sufficient space for the volume expansion/contraction of the cathodes during lithium insertion/extraction on cycling. Finally, carbon-coating/wiring on the Li_2MnSiO_4 nanocrystals helps to improve the electrical conductivity in the cathode.

2.2. Electrochemical Performance

The Li_2MnSiO_4/C cathodes were evaluated in coin cells with $LiPF_6$/EC+DEC electrolyte and lithium metal anodes between 1.5 and 4.8 V. Because it has been reported that a higher temperature is beneficial to overcome the extremely low reaction kinetics of Li_2MnSiO_4 cathodes,[20a,21b] the cells were tested at 45 and 55 °C. **Figure 6**a,b shows the initial voltage-capacity profiles and cycling performances at 45 °C. The initial charge and discharge capacities at C/10 (16 mA g^{-1}, 1 C rate is defined as charge/discharge of one lithium per formula in one hour) are 180 and 140 mAh g^{-1}, respectively. The irreversible capacity is possibly due to the formation of the solid electrolyte interphase (SEI).

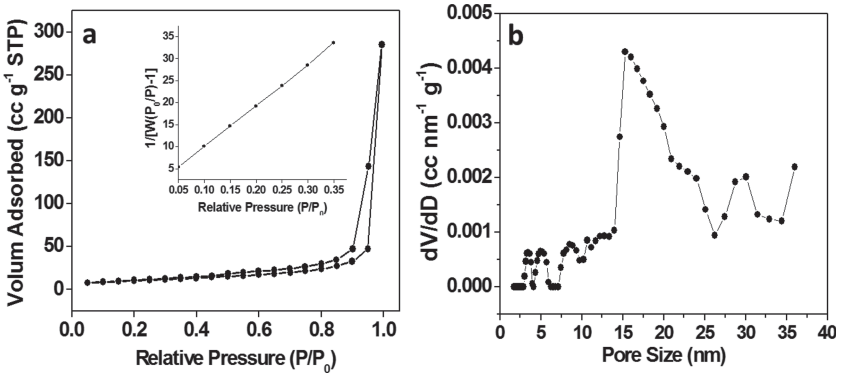

Figure 5. a) N_2 adsorption isotherm (inset: BET plot) and b) pore size distribution curve based on QS-DFT calculation.

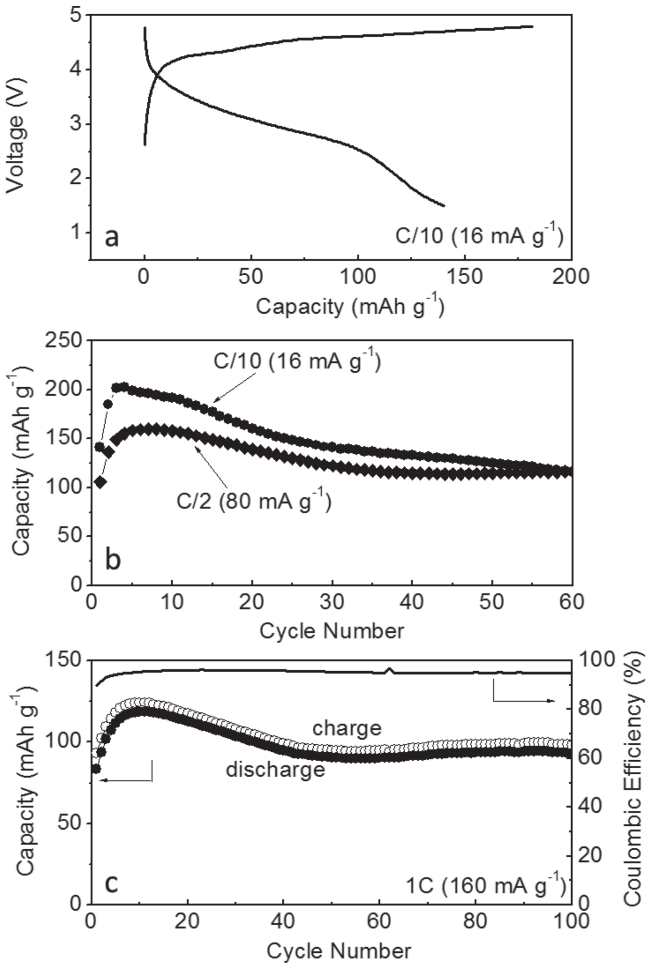

Figure 6. Electrochemical performance of the Li_2MnSiO_4/C cathodes at 45 °C: a) initial charge-discharge profile at C/10, b) cycling performance at C/10 and C/2, c) cycling performance and Coulombic efficiency over 100 cycles at 1 C rate.

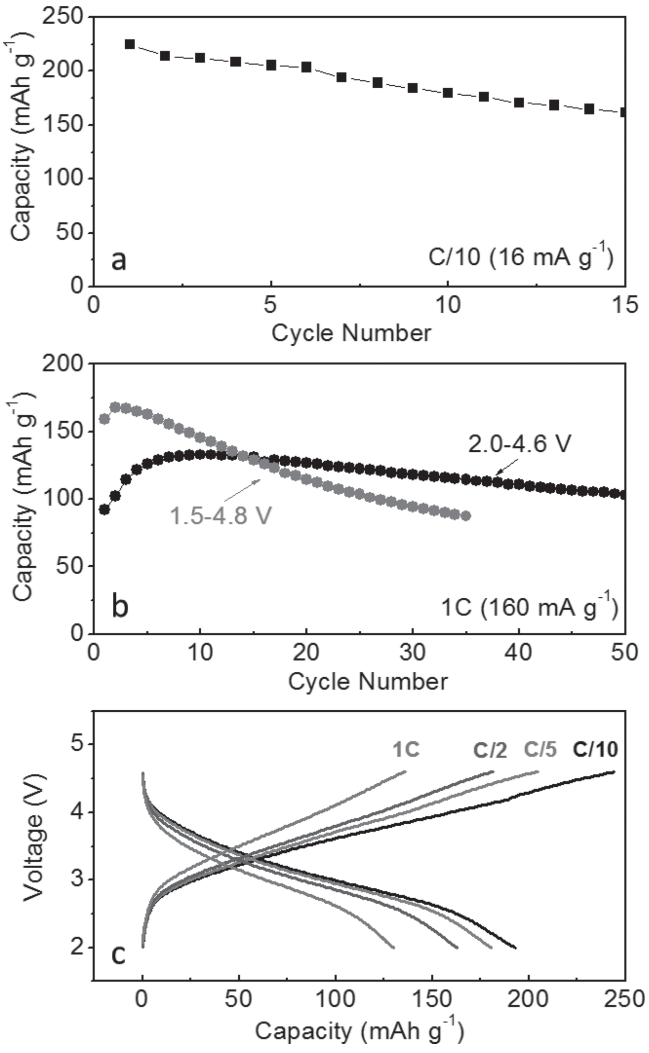

Figure 7. Electrochemical performances of the Li_2MnSiO_4/C cathodes at 55 °C: a) cycling performance at C/10 and 1.5–4.8 V, b) cut-off voltage influence on cycling at 1C rate, c) the highest capacities obtained at various rates.

The cell discharge capacity reaches a maximum of 200 mAh g^{-1} on the 3rd cycle, suggesting ≈1.2 lithium ions per formula unit are reinserted into the structure. At more practical current rates of C/2 and 1 C (80 and 160 mA g^{-1}), the highest capacities appearing on the 7th and 10th cycle are 160 and 119 mAh g^{-1}, respectively. These two cells exhibit excellent cycling stability as shown in Figure 6b,c. For example, the cell tested at 1 C has an average capacity of ≈95 mAh g^{-1} after 40 cycles as well as a high coulombic efficiency of 95%. The capacity retention over 100 cycles for this cell is 112% or 78% based on the initial and the highest capacity values, respectively, which is among one of the best cycling performance reported so far for Li_2MnSiO_4 cathodes.[5b,7,20–22,44] Capacity-increase during the first few cycles is observed for all the cells, which is probably a result of the relatively thick carbon-layers on the surface of Li_2MnSiO_4, as evidenced by the TEM image. As the sample is cycled, smooth lithium-diffusion pathways may be created and improved, resulting in an increase in the electrochemical utilization of the active material and an increase in capacity.

At a higher temperature of 55 °C, the first discharge capacity increases to 225 mAh g^{-1} (**Figure 7**a) at C/10 rate, which corresponds to ≈ 70% of the theoretical capacity (330 mAh g^{-1}). However, the capacity fading is relatively faster than that of the cell tested at 45 °C. This is possibly because of the instability of the carbonate-based electrolytes at the high operating voltage of up to 4.8 V. Figure 7b compares the stability of the cells cycled at different voltage windows. At 55 °C and 1 C rate, the highest discharge capacities are ≈170 and 133 mAh g^{-1}, respectively, at 1.5–4.8 V and 2.0–4.6 V. However, the cell tested at the narrow voltage window shows much improved stability. Based on the highest capacity, the capacity retention after 50 cycles for the 2.0–4.6 V window is 77% (Figure 7b, black curve), while it is only 52% after 35 cycles for the 1.5–4.8 V window (Figure 7b, red curve). Figure 7c shows the charge-discharge curves at various rates at 55 °C within the voltage window of 2.0–4.6 V. The capacity at C/10 is 193 mAh g^{-1}, ≈14% lower than that of the cell discharging down to 1.5 V. However, these cells at 55 °C in Figure 7c exhibit reduced polarization than those tested at 45 °C, possibly due to enhanced reaction kinetics.

It is worth noting that the capacity fading for Li_2MnSiO_4 cathodes comes from the inherent electrochemical instability of the material such as the Jahn-Teller distortion of the Mn^{3+} ion[7] and structural changes upon cycling.[45,46] The ultimate solution probably relies on partial replacement of Mn^{2+} with other metal ions to stabilize the local environment of Mn^{3+}, as demonstrated by previous work.[12,13] However, recent computational studies have also pointed out that the performance of Li_2MnSiO_4 cathodes also strongly depends on the preparation approaches, which influence the crystalline structure, particle size, etc. For example, excessive ball-milling of this material may cause structural damage and instability, although large grain size impedes ion transfer.[47] Li/Mn antisite defects in the samples is another factor that affects lithium-ion migration and phase transformation.[32] On the other hand, our work has demonstrated that the Li_2MnSiO_4 cathode with appropriate optimization can extend cycling life with stable capacities up to 100 cycles.

3. Conclusions

In summary, Li_2MnSiO_4/C nanocomposite with ordered macroporosity and in-situ carbon coating has been prepared and investigated as a cathode material for lithium-ion batteries. The unique bimodal macro/mesoporous structure facilitates electrical and ionic transport, allows fast electrolyte permeation within the cathodes, and provides space to suppress the volume expansion/contraction and the influence of active material growth. As a result, the Li_2MnSiO_4/C nanocomposite exhibits a high discharge capacity of 200 mAh g^{-1} at 45 °C and C/10 rate. At a more practical rate of 1 C, it shows excellent cycling stability with a capacity retention of 106% (based on the initial discharge capacity) or 78% (based on the highest discharge capacity) after 100 cycles, representing one of the best cycling performances reported for Li_2MnSiO_4 cathodes. The capacity could be further increased to 225 mAh g^{-1} at 55 °C, but the electrode degradation is faster than that at 45 °C. Examination of the cycling behavior with different cutoff voltages indicates better cycling stability at a narrower voltage window at 55 °C.

4. Experimental Section

PMMA Colloidal Crystals:[48] The PMMA template was prepared by polymerizing methyl methacrylate (MMA) monomer with 2,2′-azobis(2-methyl propionamidine) dihydrochloride as the initiator. Typically, 100 mL of MMA monomer was first added into 500 mL of deionized (DI) water in a three-neck flask under Ar flow. After being stirred and heated at 70 °C for 30 min, 0.5 g of 2,2′-azobis(2-methyl propionamidine) dihydrochloride was added to initiate the polymerization of MMA. The clear solution turned to a milk-like colloidal suspension in a few minutes, indicating the formation of PMMA sub-micron spheres. The reaction was held for ≈2 h, and then the PMMA was filtered, washed, and re-dispersed in DI water. In order to obtain the PMMA colloidal crystals, the colloidal suspension was transferred to petri dishes and heated at 60 °C overnight.

Phenolic Resin:[43,49] 6.1 g of phenol was melted at 40 °C and stirred with 1.0 g of 20 wt% NaOH solution for 10 min. Next, 10.5 g formalin was added and stirred for another 50 min at 65 °C. After being cooled down to room temperature, the pH of the mixture was neutralized to ≈7.0. Water was then removed by evacuation at room temperature to obtain a light-yellow PF gel. Finally, it was dissolved in ethanol to form a 50 wt% PF solution.

Li_2MnSiO_4/C: The precursor solution containing Li^+, Mn^{2+}, and Si^{4+} with a molar ratio of 2:1:1 was first prepared. Briefly, 2.08 g of tetraethyl orthosilicate (TEOS) was dissolved in a solution of 1.2 mL of DI water and 0.5 mL of 0.2 M HCl under vigorous stirring. Next, 1.4 g of $LiNO_3$, 2.5 g of $Mn(NO_3)_2{\cdot}4H_2O$, and 1.0 g of PF sol were added to this solution in sequence. The mixture was stirred for another 1 h to obtain a clear viscous solution. The filtration of the template was achieved by partially immersing the PMMA crystals into the above solution for a few hours. The small pieces of PMMA were then carefully taken out and wiped with tissue paper to remove excess liquid on the surface of the template. They were then dried in air at 50 °C for 5 h and subsequently treated at 100 °C for 24 h to finish the thermopolymerization of PF. Finally, the PMMA/precursors composite was pyrolyzed at 700 °C under Ar atmosphere.

Material Characterization: Surface area and pore size of the Li_2MnSiO_4/C nanocomposite were determined from nitrogen adsorption and desorption isotherms, respectively, performed on a Quantachrome Autosorb iQ-MP instrument at 77 K. Before the measurement, the samples were degassed at 100 °C with a vacuum line. The total pore volume of the Li_2MnSiO_4/C composite was calculated at a relative pressure of 0.995 (P/P_0). The specific surface area, pore size distribution, and pore volumes were determined by the BET theory and the QS-DFT model from the adsorption branch of the isotherms. FE-SEM and elemental maps were carried out on a Hitachi S5500 STEM, and TEM images were acquired on a Hitachi JEOL JEM-2010F equipment. The composition of the Li_2MnSiO_4 composite was confirmed by the Varian 715-EIS inductively plasma coupled analyzer (ICP). TGA data were collected with the NETZSCH STA 449 instrument. Raman analysis was performed with a Renishaw InVia system.

Electrochemistry: The Li_2MnSiO_4/C cathode materials were cast from N-methyl-2-pyrrolidone (NMP) onto aluminum collectors using polyvinylidene fluoride (PVDF) as the binder. The formula of the Li_2MnSiO_4/C electrode is Li_2MnSiO_4/C:Super P:PVDF = 80:10:10 with a typical electrode loading of ≈3 mg cm^{-2}. The CR 2032 coin cells were fabricated in an Ar-filled glove box using 1 M $LiPF_6$ in ethylene carbonate (EC) and diethyl carbonate (DEC) (1:1 vol/vol) electrolyte, a metallic lithium negative electrode, and Celgard 2500 polypropylene separator. Cells were cycled with an Arbin cycler in an oven at 45 or 55 °C.

Supporting Information

Supporting Information is available from the Wiley Online Library or from the author.

Acknowledgements

This work was supported by the Assistant Secretary for Energy Efficiency and Renewable Energy, the Office of Vehicle Technologies of the U.S. Department of Energy under Contract No. DE-AC02–05CH11231, Subcontract No. 7000389 under the Batteries for Advanced Transportation Technologies (BATT) Program.

Received: February 21, 2014
Revised: April 4, 2014
Published online: June 6, 2014

[1] H. Makeki, S. A. Hallaj, J. R. Selman, R. B. Dinwiddie, H. Wang, *J. Electrochem. Soc.* **1999**, *146*, 947.
[2] R. V. Chebiam, F. Prado, A. Manthiram, *Chem. Mater.* **2001**, *13*, 2951.
[3] C. Masquelier, L. Croguennec, *Chem. Rev.* **2013**, *113*, 6552.
[4] M. S. Whittingham, *Chem. Rev.* **2004**, *104*, 4271.

[5] a) A. Nytén, A. Abouimrane, M. Armand, T. Gustafsson, J. O. Thomas, *Electrochem. Commun.* **2005**, *7*, 156; b) R. Dominko, M. Bele, M. Gaberšček, A. Meden, M. Remškar, J. Jamnik, *Electrochem. Commun.* **2006**, *8*, 217; c) C. Lyness, B. Delobel, A. R. Armstrong, P. G. Bruce, *Chem. Commun.* **2007**, 4890.
[6] D. Lv, W. Wen, X. Huang, J. Bai, J. Mi, S. Wu, Y. Yang, *J. Mater. Chem.* **2011**, *21*, 9506.
[7] T. Muraliganth, K. R. Stroukoff, A. Manthiram, *Chem. Mater.* **2010**, *22*, 5754.
[8] D. Rangappa, K. D. Murukanahally, T. Tomai, A. Unemoto, I. Honma, *Nano Lett.* **2012**, *12*, 1146.
[9] Z. Chen, S. Qiu, Y. Cao, J. Qian, X. Ai, K. Xie, X. Hong, H. Yang, *J. Mater. Chem. A* **2013**, *1*, 4988.
[10] D. Lv, J. Bai, P. Zhang, S. Wu, Y. Li, W. Wen, Z. Jiang, J. Mi, Z. Zhu, Y. Yang, *Chem. Mater.* **2013**, *25*, 2014.
[11] Z. Gong, Y. Yang, *Energy Environ. Sci.* **2011**, *4*, 3223.
[12] R. Chen, R. Heinzmann, S. Mangold, V. S. K. Chakravadhanula, H. Hahn, S. Indris, *J. Phys. Chem. C* **2013**, *117*, 884.
[13] R. Dominko, C. Sirisopanaporn, C. Masquelier, D. Hanzel, I. Arcon, M. Gaberscek, *J. Electrochem. Soc.* **2010**, *157*, A1309.
[14] A. R. Armstrong, C. Lyness, M. Ménétrier, P. G. Bruce, *Chem. Mater.* **2010**, *22*, 1892.
[15] Z. L. Gong, Y. X. Li, Y. Yang, *J. Power Sources* **2007**, *174*, 524.
[16] G. He, G. Popov, L. F. Nazar, *Chem. Mater.* **2013**, *25*, 1024.
[17] M. E. Arroyo-de Dompablo, M. Armand, J. M. Tarascon, U. Amador, *Electrochem. Commun.* **2006**, *8*, 1292.
[18] G. Zhong, Y. Li, P. Yan, Z. Liu, M. Xie, H. Lin, *J. Phys. Chem. C* **2010**, *114*, 3693.
[19] M. S. Islam, R. Dominko, C. Masquelier, C. Sirisopanaporn, A. R. Armstrong, P. G. Bruce, *J. Mater. Chem.* **2011**, *21*, 9811.
[20] a) R. Dominko, *J. Power Sources* **2008**, *184*, 462; b) A. Kokalj, R. Dominko, G. Mali, A. Meden, M. Gaberscek, J. Jamnik, *Chem. Mater.* **2007**, *19*, 3633.
[21] a) S. Aono, T. Tsurudo, K. Urita, I. Moriguchi, *Chem. Commun.* **2013**, *49*, 2939; b) R. Dominko, M. Bele, A. Kokalj, M. Gaberšček, J. Jamnik, *J. Power Sources* **2007**, *174*, 457; c) A. Bhaskar, M. Deepa, T. N. Rao, U. V. Varadaraju, *J. Electrochem. Soc.* **2012**, *159*, A1954; d) Z. Hu, K. Zhang, H. Gao, W. Duan, F. Cheng, J. Liang, J. Chen, *J. Mater. Chem. A* **2013**, *1*, 12650; e) H. Gong, Y. Zhu, L. Wang, D. Wei, J. Liang, Y. Qian, *J. Power Sources* **2014**, *246*, 192.
[22] V. Aravindan, K. Karthikeyan, K. S. Kang, W. E. Yoon, W. S. Kim, Y. S. Lee, *J. Mater. Chem.* **2011**, *21*, 2470.
[23] Y. Zhao, C. Wu, J. Li, L. Guan, *J. Mater. Chem. A* **2013**, *1*, 3856.
[24] S. Zhang, C. Deng, F. L. Liu, Q. Wu, M. Zhang, F. L. Meng, H. Gao, *J. Electroanal. Chem.* **2012**, *689*, 88.
[25] A. Vu, Y. Qian, A. Stein, *Adv. Energy Mater.* **2012**, *2*, 1056.
[26] K. T. Lee, J. C. Lytle, N. S. Ergang, S. M. Oh, A. Stein, *Adv. Funct. Mater.* **2005**, *15*, 547.
[27] H. Yan, S. Sokolov, J. C. Lytle, A. Stein, F. Zhang, W. H. Smyrl, *J. Electrochem. Soc.* **2003**, *150*, A1102.
[28] J. S. Sakamoto, B. Dunn, *J. Mater. Chem.* **2002**, *12*, 2859.
[29] D. Tonti, M. J. Torralvo, E. Enciso, I. Sobrados, J. Sanz, *Chem. Mater.* **2008**, *20*, 4783.
[30] C. M. Doherty, R. A. Caruso, B. M. Smarsly, C. J. Drummond, *Chem. Mater.* **2009**, *21*, 2895.
[31] A. Vu, A. Stein, *Chem. Mater.* **2011**, *23*, 3237.
[32] C. A. J. Fisher, N. Kuganathan, M. S. Islam, *J. Mater. Chem. A* **2013**, *1*, 4207.
[33] M. Kuezma, S. Devaraj, P. Balaya, *J. Mater. Chem.* **2012**, *22*, 21279.
[34] S. J. Kim, J. Suk, Y. J. Yun, H.-K. Jung, S. Choi, *Phys. Chem. Chem. Phys.* **2014**, *16*, 2085.
[35] B. Shao, I. Taniguchi, *Electrochimica Acta* **2014**, *128*, 156.
[36] S. Devaraj, M. Kuezma, C. T. Ng, P. Balaya, *Electrochimica Acta* **2013**, *102*, 290.
[37] J. Liu, H. Xu, X. Jiang, J. Yang, Y. Qian, *J. Power Sources* **2013**, *231*, 39.
[38] K. Karthikeyan, V. Aravindan, S. B. Lee, I. C. Jang, H. H. Lim, G. J. Park, M. Yoshio, Y. S. Lee, *J. Power Sources* **2010**, *195*, 3761.
[39] V. Aravindan, K. Karthikeyan, S. Ravi, S. Amaresh, W. S. Kim, Y. S. Lee, *J. Mater. Chem.* **2010**, *20*, 7340.
[40] J. Schuster, G. He, B. Mandlmeier, T. Yim, K. T. Lee, T. Bein, L. F. Nazar, *Angew. Chem. Int. Ed.* **2012**, *51*, 3591.
[41] A. Vu, A. Stein, *J. Power Sources* **2014**, *245*, 48.
[42] N. D. Petkovich, S. G. Rudisill, B. E. Wilson, A. Mukherjee, A. Stein, *Inorg. Chem.* **2014**, *53*, 1100.
[43] R. Liu, Y. Shi, Y. Wan, Y. Meng, F. Zhang, D. Gu, Z. Chen, B. Tu, D. Zhao, *J. Am. Chem. Soc.* **2006**, *128*, 11652.
[44] a) X. Jiang, H. Xu, J. Liu, Y. Qian, *Mater. Lett.* **2013**, *113*, 9; b) R. J. Gummow, Y. He, *J. Power Sources* **2014**, *253*, 315; c) M. Moriya, M. Miyahara, M. Hokazono, H. Sasaki, A. Nemoto, S. Katayama, Y. Akimoto, S. Hirano, *J. Electrochem. Soc.* **2014**, *161*, A97.
[45] Y.-X. Li, Z.-L. Gong, Y. Yang, *J. Power Sources* **2007**, *174*, 528.
[46] D. Sun, H. Wang, P. Ding, N. Zhou, X. Huang, S. Tan, Y. Tang, *J. Power Sources* **2013**, *242*, 865.
[47] M. M. Kalantarian, S. Asgari, P. Mustarelli, *J. Mater. Chem. A* **2013**, *1*, 2847.
[48] R. C. Schroden, M. Al-Daous, S. Sokolov, B. J. Melde, J. C. Lytle, A. Stein, M. C. Carbajo, J. T. Fernández, E. E. Rodríguez, *J. Mater. Chem.* **2002**, *12*, 3261.
[49] G. He, X. Ji, L. Nazar, *Energy Environ. Sci.* **2011**, *4*, 2878.